ACS APPLIED MATERIALS & INTERFACES

Research Article

www.acsami.org

Porous α-MoO_3/MWCNT Nanocomposite Synthesized via a Surfactant-Assisted Solvothermal Route as a Lithium-Ion-Battery High-Capacity Anode Material with Excellent Rate Capability and Cyclability

Feng Ma,[†] Anbao Yuan,*[,†] Jiaqiang Xu,*[,†] and Pengfei Hu[‡]

[†]Department of Chemistry, College of Sciences, and [‡]Instrumental Analysis & Research Center, Shanghai University, Shanghai 200444, China

Supporting Information

ABSTRACT: A high-performance α-MoO_3/multiwalled carbon nanotube (MWCNT) nanocomposite material is synthesized via a novel surfactant-assisted solvothermal process followed by low-temperature calcination. Its structure, composition, and morphology are characterized by X-ray diffraction, X-ray photoelectron spectroscopy, energy-dispersive X-ray spectroscopy, carbon element analysis, nitrogen adsorption−desorption determination, scanning electron microscopy, and transmission electron microscopy techniques. Its electrochemical performance as a high-capacity lithium-ion-battery anode material is investigated by cyclic voltammetry, electrochemical impedance spectroscopy, and galvanostatic discharge/recharge methods. This composite material exhibits not only high capacity but also excellent rate capability and cyclability. For example, when the discharge/charge current density is increased from 0.1 to 2 A g^{-1}, the reversible charge capacity is only decreased from 1138.3 to 941.4 mAh g^{-1}, giving a capacity retention of 82.7%. Even if it is cycled at a high current density of 20 A g^{-1}, a reversible charge capacity of 490.2 mAh g^{-1} is still retained, showing a capacity retention of 43.1%. When it is repeatedly cycled at a current of 0.5 A g^{-1}, the initial reversible charge capacity is 1041.1 mAh g^{-1}. A maximum charge capacity of 1392.2 mAh g^{-1} is achieved at the 292th cycle. After 300 cycles, a high charge capacity of 1350.3 mAh g^{-1} is maintained. Enhancement of the electrical conduction contributed by the MWCNT composite component as well as the loose and porous texture of the MoO_3/MWCNT composite is suggested to be responsible for the excellent performance.

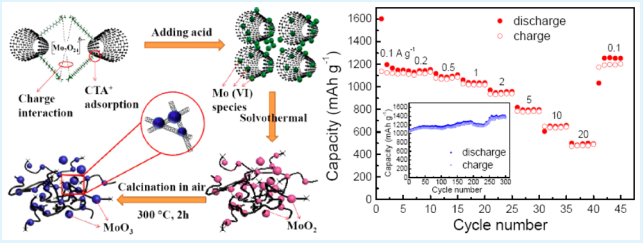

KEYWORDS: *crystalline α-MoO_3 nanoparticles, multiwalled carbon nanotubes, composite, lithium-ion battery, conversion-type anode*

1. INTRODUCTION

With the ever-increasing attention to environmental and resource issues, clean, sustainable, and renewable energy sources such as solar energy, wind energy, tidal energy etc., are regarded as promising substitutions for traditional fossil fuels. However, large-scale applications of electric energy storage and release technologies such as smart grid, storage of renewable energies, fully electric vehicles, and plug-in hybrid electric vehicles still remain challenges. Lithium-ion batteries (LIBs) have been widely used in various fields such as mobile telephones, laptop computers, and other small portable appliances. Nevertheless, the performances of LIBs need to be improved to meet the rigorous requirements regarding high energy and power densities and long service life. As we all know, energy and power densities are related to an electrode's specific capacity and a battery's working voltage as well as electrode reaction kinetics. Commercially used graphite suffers from a relatively low capacity (theoretical capacity of 372 mAh g^{-1}) and a large initial capacity loss. Conversion-type transition-metal oxides such as Co_3O_4,[1] Fe_2O_3,[2] NiO,[3] and MoO_2[4,5] and alloying-type materials like Si[6] and Sn[7] have been considered as promising high-capacity anode materials for LIBs. Such an anode would be coupled with a high-voltage cathode (e.g., spinel-type $LiNi_{0.5}Mn_{1.5}O_4$ with a high potential of ca. 4.7 V vs Li^+/Li and a theoretical capacity of 146.7 mAh g^{-1})[8] to construct a rechargeable full battery with relatively higher energy and power densities due to the advisible integration of a high-capacity anode and a high-voltage cathode in a single full cell.

Molybdenum trioxide (MoO_3), one of the most environmentally friendly and cost-affordable transition-metal oxides, has been applied as an active component of composite materials or as a pristine material for aqueous supercapacitor electrodes,[9,10] nonaqueous thin-film supercapacitor electrodes,[11] aqueous LIB intercalation anodes,[12] and nonaqueous LIB intercalation cathodes (operated in the potential range of 1.5−4, 1.5−3.5, or 1.5−3.25 V vs Li^+/Li).[13−17] In addition, MoO_3 can also be used as a conversion-type anode material for LIBs

Received: May 7, 2015
Accepted: July 1, 2015
Published: July 1, 2015

ACS Publications © 2015 American Chemical Society

DOI: 10.1021/acsami.5b03953
ACS Appl. Mater. Interfaces 2015, 7, 15531−15541

owing to its high theoretical capacity of 1117 mAh g^{-1} based on the so-called conversion reaction (typically operating in the potential range of 0−3 V vs Li^+/Li).[18−20] Nanostructured MoO_3 with a high surface area has drawn researchers' attention because it can promise a shorter diffusion path and better electrolyte penetration compared to bulk MoO_3. In addition, nanostructures can alleviate the strain caused by lithiation and, hence, can enhance the cycling performance. Already reported nanostructured MoO_3 conversion-anode materials include nanoparticles,[21] nanobelts,[22,23] nanofibers,[24] nanowire bundles,[25] nanorods[26] and yolk−shell microspheres.[27]

MoO_3-based composites with highly conductive carbonaceous materials such as reduced graphene oxide[28,29] and carbon nanotubes (CNTs)[30] can attain obviously improved electrochemical performances as conversion-anode materials for LIBs. CNT is known to be outstanding in its excellent electric conductivity, high aspect ratio, and large specific surface area and is often used as a conductive component for the preparation of composite electrode materials.[31,32] Of course, it is also expected to obtain MoO_3-based composite electrode materials with improved performance. A variety of approaches have been attempted to obtain MoO_3/CNT composites. For example, binder-free MoO_3/MWCNT thin-film electrodes were prepared by a magnetron sputtering technique for nonaqueous supercapacitor applications.[33] A MoO_3/CNT reciprocal multilayer on a nickel foam substrate was fabricated by an alternate electrodeposition method for an aqueous asymmetric pseudocapacitor anode.[34] MoO_3 nanodots/MWCNT hybrids were achieved by the sonochemical method using $MoCl_5$ as the molybdenum source (deposition of MoO_3 nanodots on the surface of CNTs) for a nonaqueous supercapacitor electrode.[35] An ultrathin MoO_3 film coated on CNTs was obtained by solution-based precipitation and post heat treatment for use as an aqueous supercapacitor electrode.[36] Nanocomposites of intertwined MWCNTs and MoO_3 nanowires were synthesized by the hydrothermal method using MoO_2 as the molybdenum precursor and H_2O_2 as the oxidant and were used as electrode materials for an aqueous supercapacitor.[37] Similarly, CNT-wired and oxygen-deficient MoO_3 nanobelts were fabricated via a hydrothermal reaction between metallic molybdenum powder and H_2O_2 followed by controlled reduction in Ar/H_2 flow to form a MoO_{3-x}/CNT composite (63 mol % MoO_3 and 37 mol % MoO_2).[30] These samples share a morphology similar to that of one-dimensional MoO_3 wired by or contacted to CNTs.

In the present work, a well-dispersed nanostructured MoO_3/MWCNT nanocomposite material with porous texture was prepared via a novel synthesis strategy involving a surfactant-assisted solvothermal process followed by low-temperature calcination in an air atmosphere. This composite material was investigated as a high-capacity conversion anode for LIBs. The basic chemical principle for synthesis of the MoO_3/CNT composite is given in the Results and Discussion section.

2. EXPERIMENTAL SECTION

2.1. Synthesis of Materials. All of the chemicals used herein are of analytical grade purchased from Sinopharm Chemical Reagent Co., Ltd. (China). Cetyltrimethylammonium bromide [CTAB; $C_{16}H_{33}(CH_3)_3NBr$, 1 g] was dissolved in a mixed solvent (18 mL of water and 9 mL of ethanol), and then a given amount (0.1 g) of multiwalled carbon nanotubes (MWCNTs; Nanjing XFNANO Materials Tech Co., Ltd., Nanjing, China) with outside diameters of 30−50 nm and lengths of 10−20 μm were dispersed in the above mixed solution under ultrasonication for 2 h. Then, a separate solution of ammonium molybdate ($(NH_4)_6Mo_7O_{24}\cdot 4H_2O$, 3/7 mmol) in deionized (DI) water (9 mL) was dropped into the above suspension under magnetic stirring. Afterward, a small amount (1.65 mL) of nitric acid (65 wt %) was added dropwise under vigorous stirring. Meanwhile, the color of the suspension changed from black to gray (due to the formation of milk-white molybdic acid hydrate). After continuous stirring for 0.5 h, the suspension was transferred into a Teflon-lined stainless steel autoclave (50 mL) and heated in an oven at 180 °C for 20 h. After cooling to room temperature, the precipitate was collected by centrifugation and then washed five times with a mixed solution of DI water and ethanol, followed by washing with absolute ethanol once again. The washed precipitate was dried at 80 °C for 12 h. Thus, a MoO_2/CNT composite (precursor) was obtained. Finally, the MoO_2/CNT precursor was placed in a tube furnace, heated in an air atmosphere from room temperature to 300 °C with a heating rate of 2 °C min^{-1}, and then kept at 300 °C for 2 h. After cooling to room temperature, a MoO_3/CNT composite material was produced. For comparison, pristine MoO_3 was also prepared with the procedure described above excluding the addition of CNTs. In addition, in order to know whether the solvothermal process has an influence on the structure and electrochemical performance of the final product, a MoO_3/CNT composite without undergoing the solvothermal process was also prepared using a similar procedure. In brief, after the addition of nitric acid and stirring for 0.5 h, the CNT-containing suspension was centrifugally separated at 3900 rpm by a centrifuge and then washed, dried, and heated at 300 °C for 2 h in an air atmosphere. Therein, for convenience, pristine MoO_3 and the MoO_3/CNT composite without the solvothermal process are denoted simply as MoO_3 and MoO_3/CNT (WST), respectively.

2.2. Characterization of Materials. X-ray diffraction (XRD) was carried out on an X-ray diffractometer (Rigaku D/max 2200, Japan) with Cu Kα radiation (40 kV/40 mA) at a scan rate of 6° min^{-1}. A X-ray photoelectron spectroscopy (XPS) study was conducted on an X-ray photoelectron spectrometer (ThermoFisher Scientific ESCALAB 250Xi, USA) with monochromatic Al Kα radiation. Morphological and microstructural observation was performed using a field-emission scanning electron microscope (Shimadzu SUPERSCAN SSX-550, Japan) and a JEOL JSM-6700F instrument (Japan) coupled with an energy-dispersive X-ray spectrometer for energy-dispersive X-ray spectrometry (EDS) mapping elemental analysis, transmission electron microscopy (TEM; JEOL JEM-200CX, Japan), and high-resolution transmission electron microscopy (HRTEM; JEOL JEM-2010F, Japan). Low-temperature nitrogen adsorption−desorption isotherms and pore-size distributions were measured at −196 °C on a surface area and porosity analyzer (Micromeritics ASAP 2020, USA). The carbon (CNTs) content was analyzed using an elemental analyzer (Elementar Analysensysteme GmbH VARIO EL III, Germany). Thermogravimetric and differential scanning calorimetric (TG−DSC) analysis was performed on a differential scanning calorimeter (Netzsch STA-409 PG/PC, Germany) with a heating rate of 10 °C min^{-1}.

2.3. Electrochemical Measurements. A working electrode was fabricated by mixing active material [MoO_3/CNT, MoO_3 (physical addition of CNTs), MoO_3, MoO_3/CNT (WST), or pure CNTs], an acetylene black conductive agent, and a sodium carboxymethyl cellulose binder in the weight ratio of 75:15:10 with a few drops of DI water. The resultant slurry was coated onto a copper foil current collector with a doctor blade and dried at 80 °C in a vacuum overnight. CR2016 coin-type half-cells were assembled in an argon-filled glovebox (Mikrouna Co., Ltd. Super 1220/750, China; with O_2 and H_2O concentrations <1 ppm) using the fabricated working electrodes and metallic lithium foil as the counter and reference electrodes and 1 M $LiPF_6$ dissolved in a mixture of ethylene carbonate, dimethyl carbonate, and methyl ethyl carbonate (1:1:1, v/v/v) as the electrolyte. For comparison with the MoO_3/CNT composite electrode, as mentioned above, a working electrode with the active material containing 81.4 wt % pristine MoO_3 and 18.6 wt % MWCNTs (physical addition) was also fabricated. For simplicity, this electrode is denoted as MoO_3 (physical addition of CNTs). Electrochemical impedance spectroscopy (EIS) and cyclic voltamme-

DOI: 10.1021/acsami.5b03953
ACS Appl. Mater. Interfaces 2015, 7, 15531−15541

try (CV) measurements were performed on a CorrTest CS330 Electrochemical Workstation (China). Galvanostatic discharge/charge tests were carried out on a Land CT2001A autocycler (China). All of the electrochemical measurements were conducted at room temperature.

3. RESULTS AND DISCUSSION

3.1. Chemical Principle for Synthesis of the MoO_3/CNT Composite. In this study, the MoO_3/CNT composite was synthesized via a two-step route. In the first step, a MoO_2/CNT composite (precursor) was obtained by a solvothermal reaction, while in the second step, the MoO_2/CNT precursor was oxidized to the MoO_3/CNT composite by heating it in an air atmosphere at a relatively low temperature of 300 °C for a short time of 2 h. It should be noted that realization of the MoO_2/CNT composite in the present work is different from those reported previously, for example, the reported preparation of a MoO_2/MWCNT hybrid.[38] In that case, the sodium dioctyl sulfosuccinate anionic surfactant adsorbed on the CNTs helps to form a W/O type reverse micelle and thus facilitates the water-soluble molybdic acid radical ions migrating into the water phase of the W/O reverse micelles. Instead, in our case, a quaternary ammonium salt-type cationic surfactant (CTAB) was used as a dispersant and a sorbate (capturer). During ultrasonication of the CNT suspension containing CTAB, some hydrophobic alkyl chains of CTA^+ ($C_{16}H_{33}(CH_3)_3N^+$) ions would contact the surface of the CNTs, while the hydrophilic groups would face the water. Thus, some CTA^+ ions could be absorbed on the surface of the CNTs, and hence the CNTs with a large aspect ratio could be well-dispersed. When ammonium molybdate [$(NH_4)_6Mo_7O_{24}{\cdot}4H_2O$] was introduced into the CNT suspension, the adhesion of molybdic acid radicals ($Mo_7O_{24}^{6-}$) onto the surface of the CNTs would take place owing to the strong electrostatic interaction and coordination between the absorbed CTA^+ cations and $Mo_7O_{24}^{6-}$ anions, forming supermolecular complexes (CNT–CTA^+–$Mo_7O_{24}^{6-}$) and, simultaneously, the system immediately changed into a sol-like suspension. Then, a small amount of nitric acid (65 wt %) was added to the suspension. In the subsequent solvothermal process, the molybdenum(VI) species could be readily reduced by the ethanol solvent, forming a MoO_2/CNT composite (precursor). Finally, the MoO_2/CNT precursor could be successfully oxidized to the MoO_3/CNT composite by calcination at a relatively low temperature of 300 °C for 2 h in an air atmosphere. At this temperature, the CNTs cannot be oxidized. The preparation procedure is outlined in Scheme 1. It should be noted that the addition of nitric acid to the system is important to the formation of MoO_2 in the solvothermal process, which will be discussed later.

3.2. Structural and Morphological Studies. Figure 1 shows the XRD patterns of MoO_3, MoO_3/CNT, and their precursors (MoO_2 and MoO_2/CNT). The diffractions of the MoO_3/CNT composite agree well with the orthorhombic α-MoO_3 [PDF 05-0508; space group *Pbnm*(62)]. Because the characteristic (002) peak of the CNTs occurring at 26.06° [see Figure S1 in the Supporting Information (SI)] is overlapped with the (040) peak of α-MoO_3, no individual (002) reflection of the CNTs could be observed in the XRD pattern of the MoO_3/CNT composite. The content of the CNTs in the MoO_3/CNT composite is 18.6 wt % (determined by carbon elemental analysis), which is in well agreement with its calculated content (18.8 wt %, estimated by calculations based on the mass balance). Compared with the MoO_3/CNT composite, the diffraction intensities of pristine α-MoO_3 are very low. Similarly, those of MoO_3/CNT (WST) are also very low (see Figure S2 in the SI).

Scheme 1. Schematic Illustration for the Preparation of the MoO_3/CNT Composite

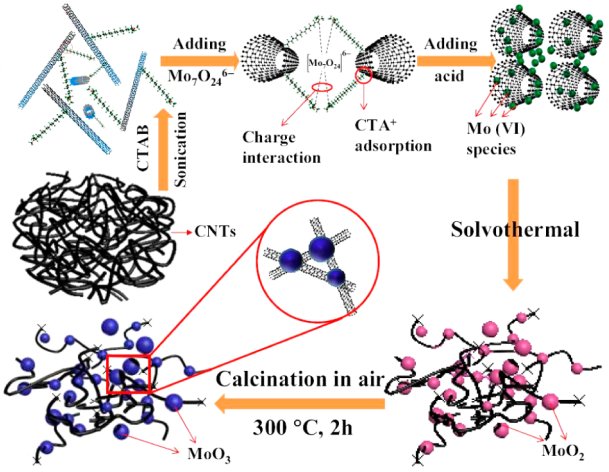

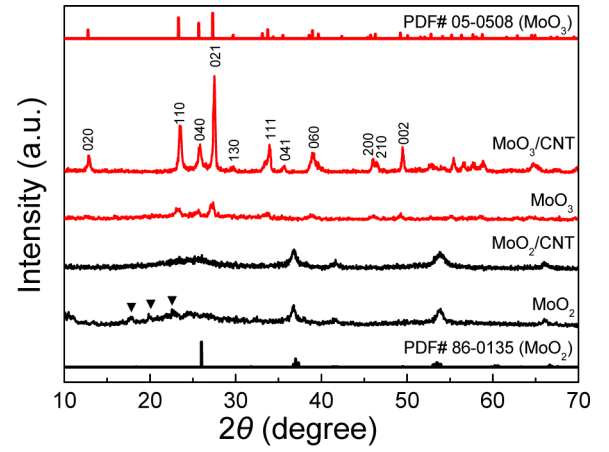

Figure 1. XRD patterns of pristine MoO_3, the MoO_3/CNT composite, and their precursors.

The XRD pattern of MoO_2/CNT (i.e., the precursor of MoO_3/CNT before calcination) is basically in line with that of MoO_2 [PDF 86-0135; space group $P2_1/c(14)$], but the peak around 26° is very weak. The XRD pattern of MoO_2 (i.e., the precursor of pristine MoO_3 before calcination) is similar to that of MoO_2/CNT, except for the additional three reflections around 20° (denoted by the solid triangles). These impurity peaks may be associated with residual CTAB species available in the solvothermal product (refer to the XRD pattern of pure CTAB powder in Figure S3 in the SI).

To study the interaction between CTA^+ and $Mo_7O_{24}^{6-}$ ions and the effect of nitric acid on the formation of MoO_2 in the solvothermal process, two distinctive experiments were conducted. In the one experiment, we found that when ammonium molybdate was added to the transparent CTAB solution (without CNTs and nitric acid), a white sol-like suspension was obtained. After centrifugation, washing, and drying, the solid precipitate was subjected to XRD analysis. In the other experiment, the white sol-like suspension (without CNTs and nitric acid) was directly subjected to the solvothermal process. After that, the solvothermal product

DOI: 10.1021/acsami.5b03953
ACS Appl. Mater. Interfaces 2015, 7, 15531–15541

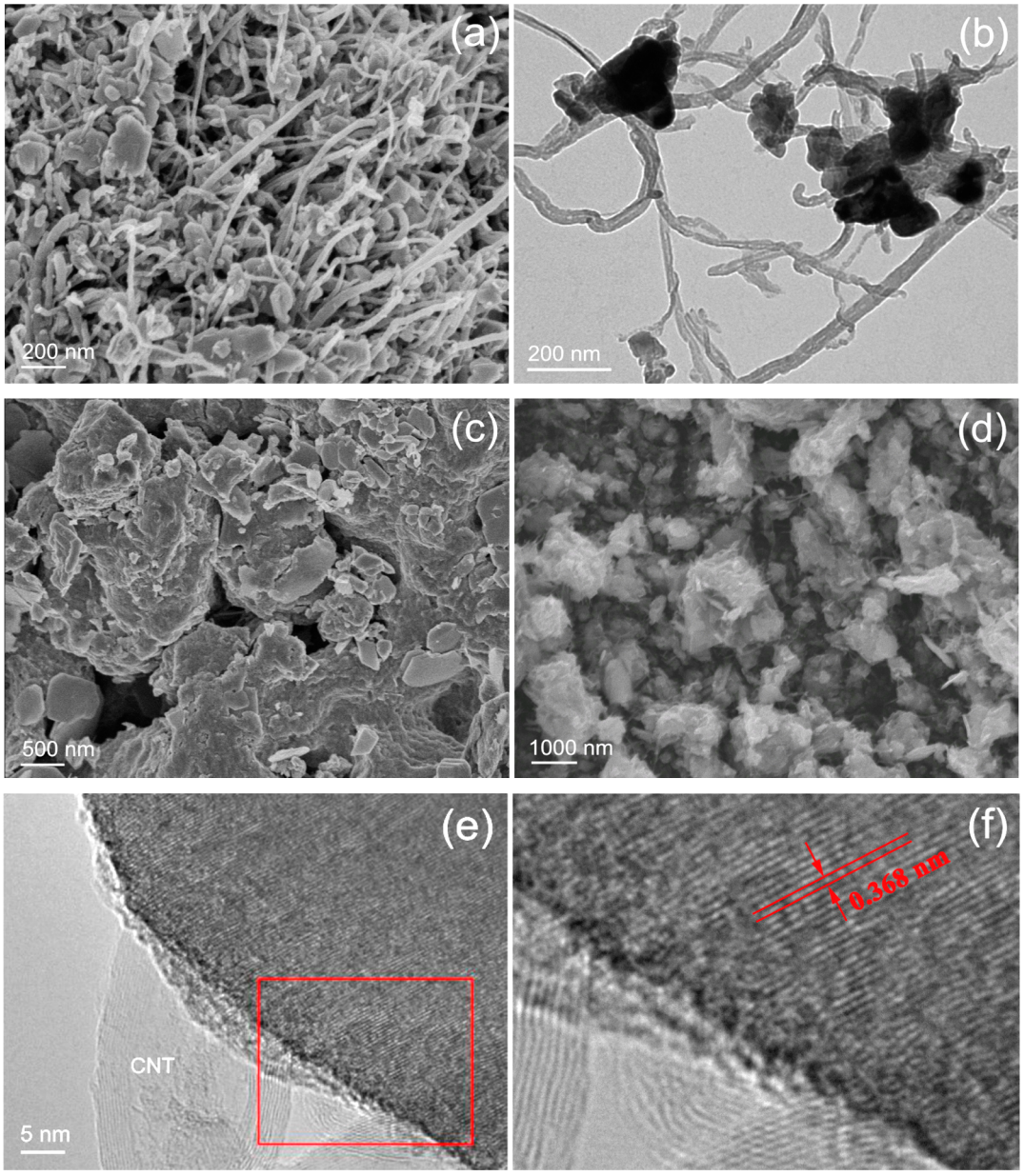

Figure 2. SEM (a) and TEM (b) images of MoO_3/CNT (the inset in part a shows a TEM image with a larger magnification). SEM images of (c) MoO_3 and (d) MoO_3/CNT (WST). (e and f) HRTEM images of MoO_3/CNT.

was centrifugally separated, washed, and dried readily for XRD analysis. XRD patterns of the two solid intermediates (before and after the solvothermal process) are shown in Figure S4a in the SI in comparison with that of the solid intermediate (without CNTs but with the previous addition of nitric acid) before the solvothermal process. As shown, the XRD pattern of the sample without nitric acid before the solvothermal process is very similar to that of the sample with nitric acid before the solvothermal process. These results confirm that the two intermediates (with or without the addition of nitric acid) before the solvothermal process are essentially the same substance (i.e., the precipitate or supermolecular complex of CTA^+–$Mo_7O_{24}^{6-}$). However, after the solvothermal process, the sol-like suspension (supermolecular complex) without nitric acid cannot change into MoO_2 (see Figure S4 in the SI). On the contrary, the sol-like suspension with nitric acid can be readily reduced to MoO_2 by ethanol (see the XRD pattern of the product in Figure 1). This result may be explained as follows: under solvothermal conditions, for the sol-like suspension with nitric acid, the hydrated H^+ ions would exchange with CTA^+ ions in the supermolecular complex of CTA^+–$Mo_7O_{24}^{6-}$, forming molybdic acid hydrate ($H_2MoO_4 \cdot nH_2O$). Simultaneously, the molybdenum(VI) species (molybdic acid hydrate) is readily reduced to MoO_2 by ethanol. The photographs of the sol-like suspension (with the addition of nitric acid before the solvothermal process) before and after centrifugal separation are shown in parts b and c of Figure S4 in the SI, respectively.

Parts a and b of Figure 2 show the scanning electron microscopy (SEM) and TEM images of the MoO_3/CNT composite, respectively, and parts c and d of Figure 2 show the SEM images of pristine MoO_3 and MoO_3/CNT (WST), respectively. For the MoO_3/CNT composite, as seen in Figure 2a, numerous MoO_3 nanoparticles are uniformly distributed in

DOI: 10.1021/acsami.5b03953
ACS Appl. Mater. Interfaces 2015, 7, 15531−15541

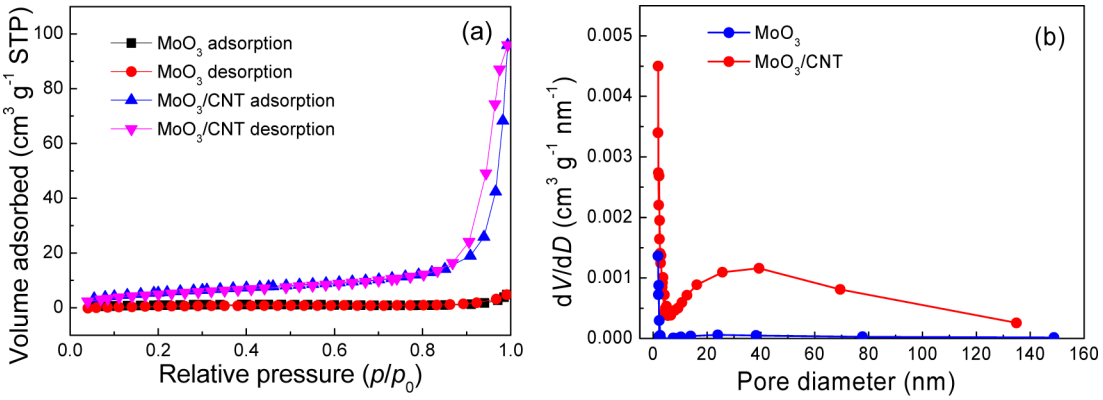

Figure 3. (a) Nitrogen adsorption−desorption isotherms and (b) pore-size distributions of MoO_3 and the MoO_3/CNT composite.

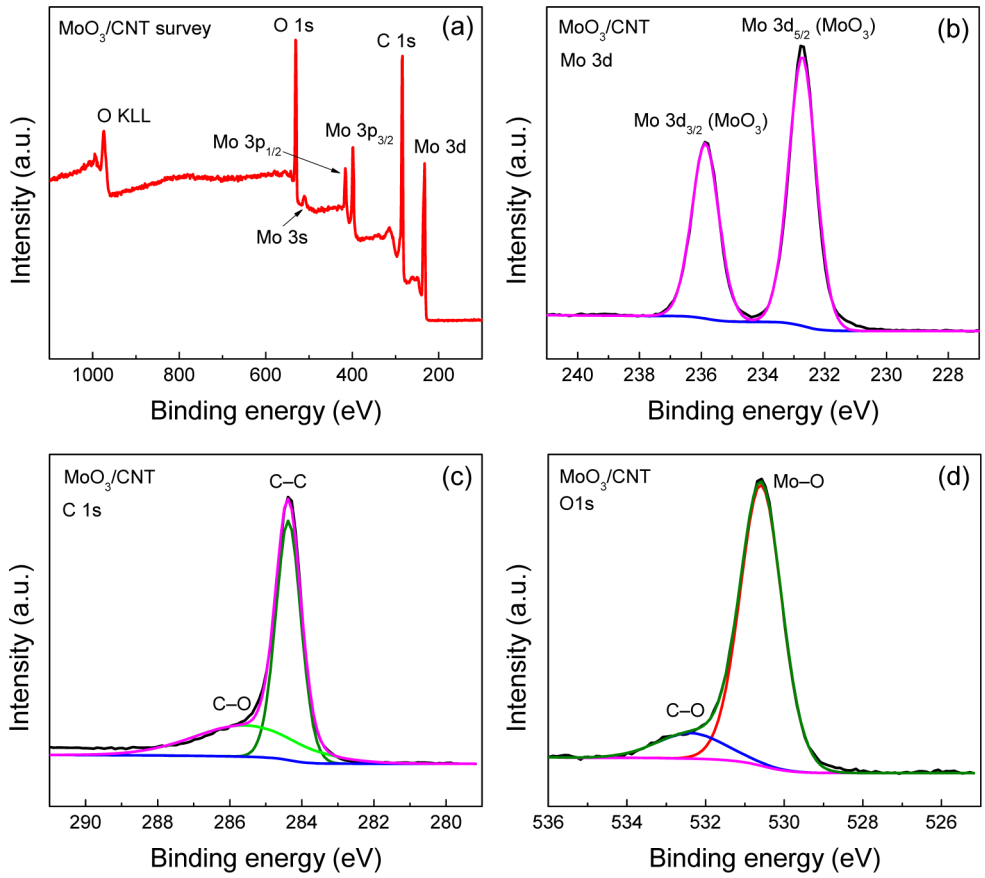

Figure 4. (a) XPS survey spectrum of the MoO_3/CNT composite and deconvoluted core-level spectra of (b) Mo 3d, (c) C 1s, and (d) O 1s.

the three-dimensional framework of intertwined CNTs. Also, we can see from the EDS mapping (Figure S5 in the SI) that the Mo, O, and C elements are uniformly distributed in the composite. As shown in Figure 2b, the MoO_3 nanoparticles are only slightly congregated into small aggregates, which are tightly combined with the CNTs, suggesting that the presence of CNTs can hinder the aggregation of MoO_3 nanoparticles to a great extent. On the contrary, the particles of pristine MoO_3 are aggregated into compact schistose-like conglomerations (Figure 2c). As for MoO_3/CNT (WST), the particles are aggregated into micron- or submicron-sized agglomerates (Figure 2d). This sample was obtained by direct calcination of the washed and dried supermolecular complexes (CNT−CTA^+−$Mo_7O_{24}^{6-}$) without the solvothermal process. These observations suggest that the solvothermal process can not only reduce the molybdenum(VI) species to molybdenum(IV) species (MoO_2) but can also result in well-dispersed small particles. Figure 2e shows the HRTEM image (lattice pattern) of a MoO_3/CNT single particle, and Figure 2f shows the enlarged lattice fringes (from the red square in Figure 2e). The measured interplanar spacing from the lattice fringes is ca. 0.368 nm, which is in agreement with that calculated from the XRD reflection of the (110) plane (d = 0.377 nm, 2θ = 23.55°; Figure 1). This result further confirms the crystalline nature of α-MoO_3 in the MoO_3/CNT composite.

The nitrogen adsorption−desorption isotherms and Barrett−Joyner−Halenda (BJH) pore-size distributions of the pristine MoO_3 and MoO_3/CNT composite materials are shown in

DOI: 10.1021/acsami.5b03953
ACS Appl. Mater. Interfaces 2015, 7, 15531−15541

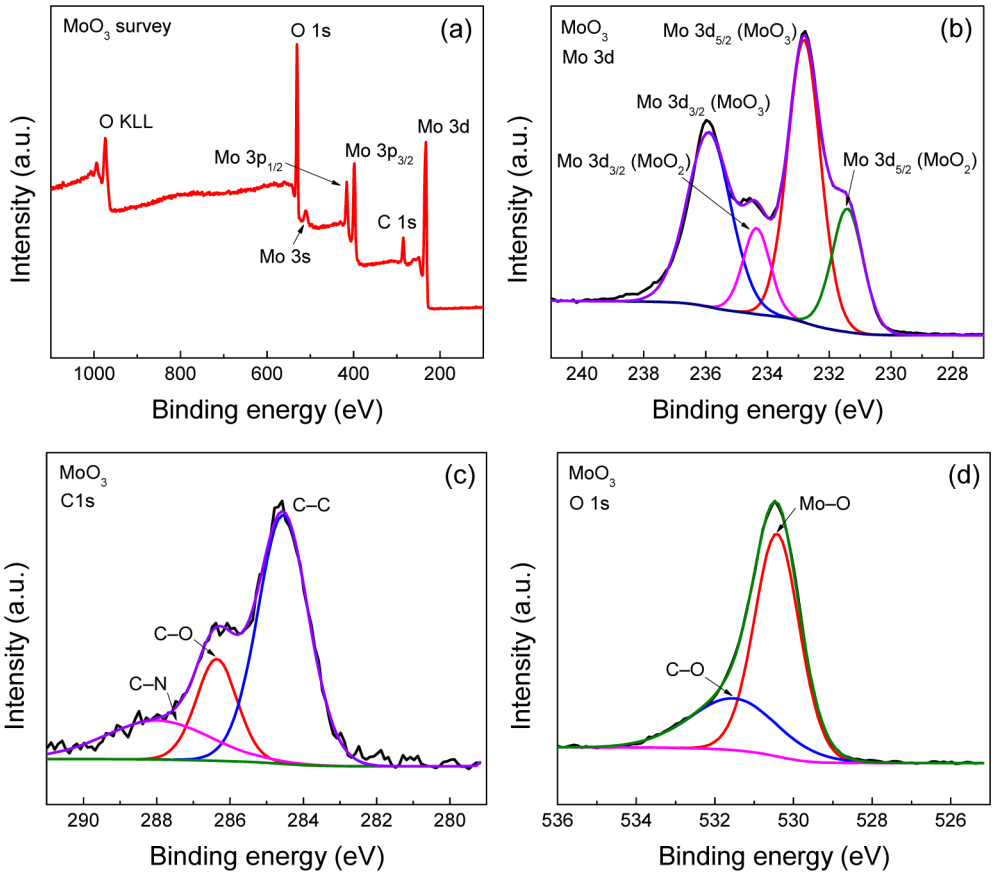

Figure 5. (a) XPS survey spectrum of MoO_3 and deconvoluted core-level spectra of (b) Mo 3d, (c) C 1s, and (d) O 1s.

Figure 3a,b, respectively. For the MoO_3 sample, when the relative pressure is lower than 0.9, almost no adsorption could be observed. When the relative pressure approaches 1.0, the adsorption quantity is very small. On the contrary, the quantity of adsorption for the MoO_3/CNT sample increases gradually with increasing relative pressure and is much larger than that of the MoO_3 sample. In addition, a hysteresis loop can be observed in the relative pressure range of 0.9−1.0. The Brunauer−Emmett−Teller surface areas of MoO_3 and MoO_3/CNT are 4.28 and 21.76 $m^2\ g^{-1}$, respectively, and the BJH total pore volumes of the two samples are 0.0064 and 0.1463 $cm^3\ g^{-1}$, respectively. As shown in Figure 3b, MoO_3/CNT exhibits a broad pore-size distribution predominantly in the pore diameter range of 5−140 nm, among which the mesopores (here, 5−50 nm) and micropores (>50 nm) contribute respectively almost equal pore volume to the total pore volume, whereas the cumulative total pore volume for MoO_3 is very small.

The XPS spectra of the MoO_3/CNT composite are shown in Figure 4. As can be seen in the XPS survey spectrum in Figure 4a, the Mo, O, and C elements are all detected and the emission of C 1s at a binding energy of 284.2 eV is intensive. The peak at 284.2 eV for C 1s and the lower satellite peak at 314.1 eV (typically the π-bond shakeup line for C 1s) should be attributed to the CNTs in the composite. The Mo 3d chemical states are well split into the Mo $3d_{3/2}$ and $3d_{5/2}$ orbitals of molybdenum(VI) centered at ca. 235.7 and 232.6 eV, respectively (Figure 3b), confirming the presence of only hexavalent molybdenum species (MoO_3) in the composite.[11,16,24,33] As can be seen from the C 1s and O 1s spectra in Figure 4c,d, the C 1s and O 1s signals show asymmetrical profiles due to the presence of oxygen-containing functional groups covalently linked to the surface C atoms of the CNTs.[29,38] Besides the C−C bond at 284.2 eV, the deconvoluted C 1s spectrum shows a band of epoxy/ether C−O groups around 285.5 eV. The O 1s core-level spectrum can be split into two deconvoluted components, i.e., the Mo−O bonds at 530.4 eV and the C−O groups at 532.3 eV. These features suggest that the surface C atom of the CNTs is most likely bonded with the surface O atom of MoO_3.

Figure 5 shows the XPS spectra of pristine MoO_3. The XPS survey spectrum of MoO_3 shown in Figure 5a is similar to that of the MoO_3/CNT composite (Figure 4a) except for the remarkably decreased C 1s peak. Here, the occurrence of the weak C 1s signal should be mainly associated with the carbon available in the conductive adhesive added for the XPS experiment and, additionally, also related to a small amount of carbonized product of the residual CTAB species. However, the Mo 3d spectrum (Figure 5b) is quite different from that of MoO_3/CNT, with the features of two additional shoulders occurring in the direction of lower binding energies to the Mo $3d_{3/2}$ and $3d_{5/2}$ orbitals of molybdenum(VI), respectively. Here, the additional deconvoluted Mo 3d signals should be ascribed to the Mo $3d_{3/2}$ and $3d_{5/2}$ orbitals of molybdenum(IV) centered at ca. 234.3 and 231.4 eV, respectively, suggesting the presence of MoO_2 in the pristine MoO_3 sample.[20,30,38] The molybdenum(IV) content in the sample can be estimated to be of ca. 21% based on the areas of the deconvoluted Mo 3d signals. The deconvoluted C 1s and O 1s core-level spectra of pristine MoO_3 are displayed in parts c and d of Figure 5,

DOI: 10.1021/acsami.5b03953
ACS Appl. Mater. Interfaces 2015, 7, 15531−15541

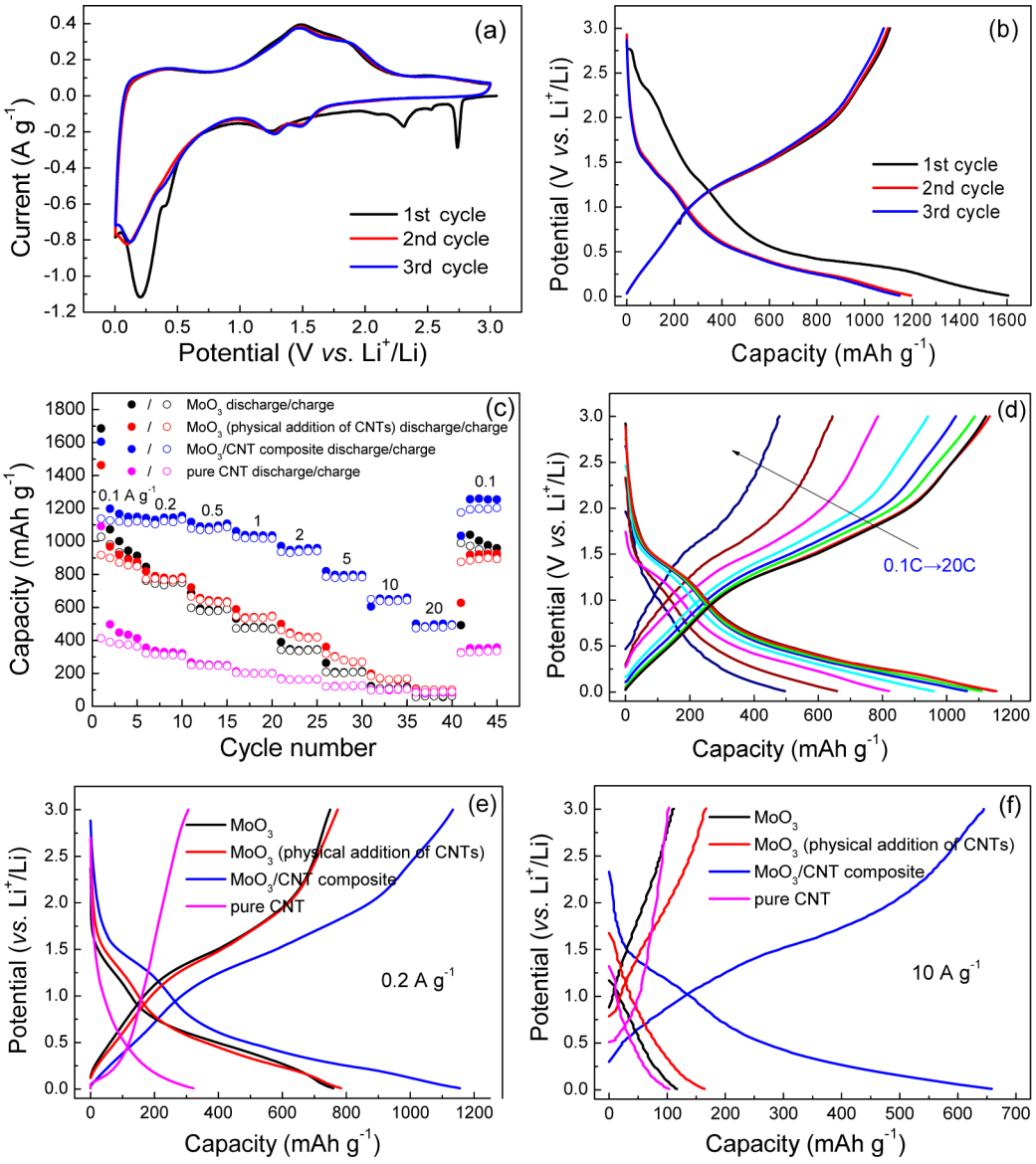

Figure 6. (a) CV of a fresh MoO_3/CNT electrode at 0.15 mV s^{-1}. (b) Discharge/charge curves of a fresh MoO_3/CNT electrode at a current density of 0.1 A g^{-1}. (c) Rate performance of MoO_3, MoO_3 (physical addition of CNTs), the MoO_3/CNT composite, and pure CNT. (d) Typical discharge/charge curves of the MoO_3/CNT composite at different current densities. (e and f) Typical discharge/charge curves of different electrodes at 0.2 and 10 A g^{-1}, respectively.

respectively, where the fitted C−N signal of the C 1s spectrum should be assigned to the C−N bond relevant to the residual CTAB species.

These observations could be explained as follows. As shown in Figure 2c, pristine MoO_3 presents the morphology of compact aggregates. This sample was obtained by calcination of the MoO_2 precursor at a relatively low temperature of 300 °C for 2 h. According to the report,[39] in the solvothermal process, some CTAB could be polymerized to long-chain species. Some CTAB and/or polymerized CTAB species may be enwrapped by the compact MoO_2 aggregates so as not to be completely washed away in the washing process. Hence, in the subsequent calcination process, it is difficult for oxygen to completely diffuse into the interior of the compact MoO_2 aggregates, and therefore some CTAB and/or polymerized CTAB species would be carbonized and some MoO_2 would not be oxidized to MoO_3. This speculation could be further confirmed by the TG−DSC measurement results (Figures S6−S8 in the SI).

3.3. Electrochemical Performance. Figure 6a shows the cyclic voltammogram of a fresh MoO_3/CNT electrode at 0.15 mV s^{-1}. In the first cathodic scan, the peaks occurring in the potential range above 1.5 V (vs Li^+/Li) are believed to be the initial reaction of lithium-ion insertion into the crystalline α-MoO_3-layered structure expressed in eq 1, while the strong cathodic peak occurring at ca. 0.2 V corresponds to the conversion reaction given in eq 2.[23,27−30] More specifically, as reported by Brezesinski et al.,[11] the cathodic peak at around 2.75 V can be attributed to an irreversible phase transition from α-MoO_3 to $Li_{0.25}MoO_3$, and the two cathodic peaks at lower potentials can be described to the charge-insertion sites of the intralayer (ca. 2.55 V) and interlayer (ca. 2.30 V), respectively.

$$MoO_3 + xLi^+ + xe^- \rightarrow Li_xMoO_3 \quad (1)$$

$$Li_xMoO_3 + (6 - x)Li^+ + (6 - x)e^- \rightarrow 3Li_2O + Mo \quad (2)$$

DOI: 10.1021/acsami.5b03953
ACS Appl. Mater. Interfaces 2015, 7, 15531−15541

In the subsequent repeated CV cycling, three pairs of redox waves with well reproducibility can be observed. The two pairs of redox peaks in the potential range of 1.0−2.25 V (i.e., the redox pair at ca. 1.3 and 1.6 V and the redox pair at ca. 1.5 and 1.9 V) are commonly recognized as being related to amorphization of the MoO_3 active material. At the end of the first cathodic conversion reaction, the crystal structure of the active material transforms into the amorphous state. As a result, MoO_3 is cycled in a quasi-amorphous state with decreased redox potentials,[25,29] while the pair of redox waves in a low potential range below 0.5 V should be ascribed to the reversible conversion reaction. After the first cycle, the cathodic conversion potential is slightly shifted to a lower potential and the cathodic peak current is obviously decreased. As shown in Figure 6b, the galvanostatic discharge/charge curves of a fresh MoO_3/CNT electrode for the initial three cycles at 0.1 A g^{-1} correspond well to the CV profiles. From the second cycle onward, the discharge profile can be roughly divided into two stages, i.e., lithium insertion into Li_xMoO_3 in the potential range above 1 V and conversion of Li_xMoO_3 into metallic Mo and Li_2O in the potential range below 1 V.

The rate performances of MoO_3, MoO_3 (physical addition of CNTs), the MoO_3/CNT composite, and pure CNT are presented in Figure 6c. The first discharge capacities of the four electrodes at 0.1 A g^{-1} are as high as 1685.4, 1462.2, 1604.5, and 1092.1 mAh g^{-1}, respectively, and the first charge capacities are 1028.3, 917.7, 1138.3, and 412.8 mAh g^{-1}, respectively, showing low Coulombic efficiencies, especially for the pure CNT electrode. The large irreversible capacity loss for the first cycle may be related to the formation of a solid−electrolyte interface (SEI) layer. From the second cycle onward, the Coulombic efficiencies are increased markedly. The MoO_3/CNT composite exhibits the highest initial reversible capacity of 1138.3 mAh g^{-1} among the four electrodes. The CNT content in the MoO_3/CNT composite is 18.6 wt %. Considering the initial reversible capacity of 412.8 mAh g^{-1} for the pure CNT electrode, the specific capacity of MoO_3 in the composite can be calculated to be 1304 mAh g^{-1}, which is higher than its theoretical capacity of 1116.7 mAh g^{-1} (based on the complete conversion of MoO_3 into metallic Mo). The phenomenon of excessive lithium-storage capacity has been found in many lithium-storage electrochemical systems based on the conversion reaction, but its mechanism is not very clear up to now. However, this phenomenon was supposed to be related to interfacial lithium storage in nanomaterials or nanocomposites.[40,41] In our case, the excessive lithium may be stored in the interface of molybdenum nanoclusters and Li_2O.

The MoO_3/CNT electrode exhibits not only the highest reversible capacity at a low current of 0.1 A g^{-1} but also a superior rate performance. For instance, when it is cycled at a current of 2 A g^{-1}, a high capacity of 941.4 mAh g^{-1} remains, giving a capacity retention of 82.7%. Even if it is cycled at a high current of 20 A g^{-1}, a relatively high capacity of 490.2 mAh g^{-1} still remains, showing a capacity retention of 43.1%. Moreover, after 40 cycles, when the current density is decreased back to 0.1 A g^{-1}, a higher capacity of 1204.1 mAh g^{-1} is regained, exhibiting a good cycling stability. The corresponding typical discharge/charge curves of the MoO_3/CNT electrode at different current densities are displayed in Figure 6d. Compared with the MoO_3/CNT composite, pristine MoO_3 and MoO_3 (physical addition of CNTs) exhibit obviously poor rate performances, although MoO_3 (physical addition of CNTs) presents a slightly lower capacity than pristine MoO_3 at 0.1 A g^{-1} but shows a little better rate performance owing to the extra addition of CNTs. These results demonstrate that the rate performance cannot be significantly improved by the physical addition of CNTs. Typical discharge/charge curves of different electrodes at 0.2 and 10 A g^{-1} are shown in Figure 6e,f, respectively. The MoO_3/CNT electrode exhibits the smallest polarization even at a high current density of 10 A g^{-1}, and hence a better rate performance is achieved, whereas the polarizations for pristine MoO_3 and MoO_3 (physical addition of CNTs) are obviously larger, especially at the increased current of 10 A g^{-1}, presenting a poor rate performance. The pure CNT electrode shows a lower lithium intercalation/deintercalation potential and a lower capacity, but its rate performance is better than those of pristine MoO_3 and MoO_3 (physical addition of CNTs) because of its superior electric conductivity.

EIS spectra of the four electrodes are displayed in Figure 7. As can be seen in the inset in the bottom middle, the ohmic

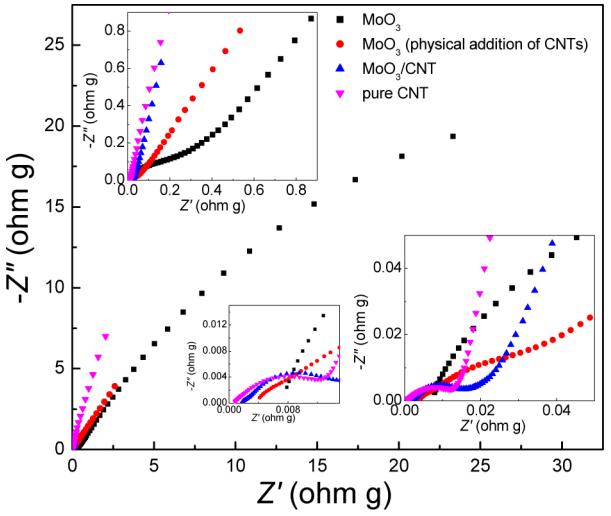

Figure 7. EISs of various electrodes measured at charged state in the frequency range of 10^5−3 × 10^{-3} Hz after the rate performance test.

resistance is in the following order: MoO_3 > MoO_3 (physical addition of CNTs) > MoO_3/CNT composite > pure CNT. The small ohmic resistance of MoO_3/CNT is due to the enhancement of the electric conductivity offered by the composite CNTs. In addition, we also can see that, in the high-frequency region, the MoO_3 (physical addition of CNTs), MoO_3/CNT composite, and pure CNT electrodes all exhibit a very small arc. By contrast, pristine MoO_3 exhibits a much larger arc in the medium-to-high-frequency region, which can be seen clearly from the insets in the bottom right and upper left. These relatively small arcs should be ascribed to the SEI layers. As shown in the inset in the bottom right, the MoO_3 (physical addition of CNTs), MoO_3/CNT composite, and pure CNT electrodes all present a semicircular arc in the medium-to-high-frequency region with the following size order: MoO_3 (physical addition of CNTs) > MoO_3/CNT composite ≈ pure CNT. Correspondingly, pristine MoO_3 presents a much larger arc in the medium-to-low-frequency region, which can be seen from the complete EIS. These semicircles should be assigned to charge-transfer resistances. The smaller charge-transfer resistance of MoO_3/CNT should be attributed to the enhancement of electrical conduction offered by the combined CNTs.

DOI: 10.1021/acsami.5b03953
ACS Appl. Mater. Interfaces 2015, 7, 15531−15541

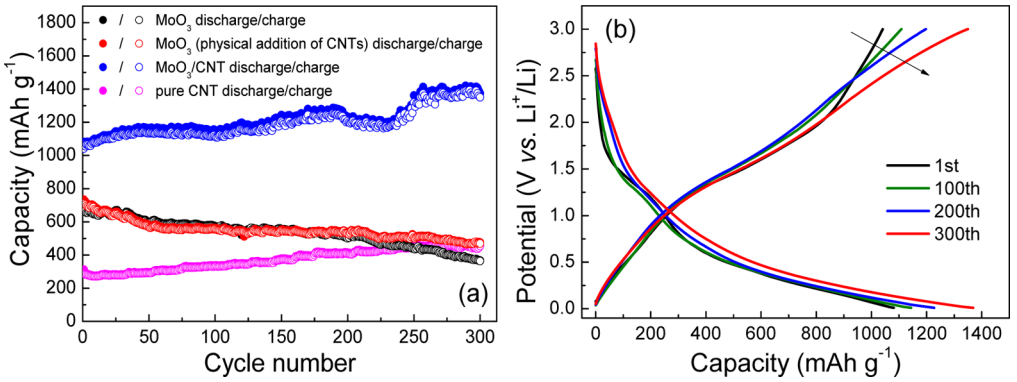

Figure 8. (a) Cycling performances of various electrodes at a current density of 0.5 A g^{-1} and (b) selected discharge/charge curves for the first, 100th, 200th, and 300th cycles of the MoO_3/CNT electrode at 0.5 A g^{-1}.

Unlike the pristine MoO_3 electrode, the other three electrodes all present an inclined line in the low-frequency region corresponding to the diffusion process. Judging from the complete EISs, the impedance of the three MoO_3-based electrodes follows the order MoO_3 > MoO_3 (physical addition of CNTs) > MoO_3/CNT composite. The excellent rate performance of the MoO_3/CNT composite (Figure 6c) should be attributed mainly to the improvement of charge transfer at the electrode−electrolyte interface caused by the tightly combined CNTs. In addition, its loose and porous texture is believed to be beneficial to electrolyte penetration into the interior of the electrode. This feature also contributes to the excellent rate performance.

Cycling performances of the pristine MoO_3, MoO_3 (physical addition of CNTs), MoO_3/CNT composite, and pure CNT electrodes at a current density of 0.5 A g^{-1} are presented in Figure 8a. As can be seen, for the three MoO_3-based electrodes, the MoO_3/CNT composite shows the highest specific capacity and the best cycling performance. Its initial charge capacity is 1041.1 mAh g^{-1}. After 190 cycles of discharge and charge, the charge capacity is increased to 1249.4 mAh g^{-1}. Since then, the charge capacity decreases first and then increases again. A maximum charge capacity of 1392.2 mAh g^{-1} is achieved at the 292th cycle. After 300 discharge/charge cycles, a high charge capacity of 1350.3 mAh g^{-1} is maintained. However, the specific capacities and cycling performances of pristine MoO_3 and MoO_3 (physical addition of CNTs) are obviously lower/poorer than those of the MoO_3/CNT composite, although the performance of MoO_3 (physical addition of CNTs) is slightly better than that of pristine MoO_3.

The charge capacity of the pure CNT electrode is increased from the initial value of 285.3 mAh g^{-1} to an end value of 453.8 mAh g^{-1} at the 300th cycle. This increment in the capacity could only contribute ca. 30 mAh g^{-1} to the capacity increment of the MoO_3/CNT composite (calculated based on the fact that the CNT content in the composite is 18.6 wt %). On the other hand, the distinct change of the discharge and charge curves of MoO_3/CNT upon repeated cycling lies in the evolution of the charge profile in the high potential range (indicated by the arrow), as shown in Figure 8b. This result may be explained as follows: upon repeated cycling, the active material would be gradually cracked into fine grains (pulverization and amorphization). Owing to the good electrical conduction and electrode kinetics of the composite material, the molybdenum species could be gradually oxidized to a higher valence state upon a charging process, and hence the capacity would increase with increasing cycle number. Additionally, the loose and porous texture of the active material could buffer the strain caused by large volume expansion/contraction during lithiation/delithiation, so as to maintain a good mechanical structure and hence a good conduction of the electrode.

To study the morphological and microstructural changes of the active material before and after cycling, HRTEM observations were conducted. Figure S9 in the SI gives a comparison of the TEM images of the MoO_3/CNT active material before and after 300 cycles at 0.5 A g^{-1}. As shown, after 300 cycles, the particles of the active material become smaller and are more uniformly dispersed on the CNTs. It can be seen from the enlarged TEM image (Figure S10a in the SI) that the particles consist of more fine particles. The HRTEM image of such a fine single active material particle (indicated by the red arrow in Figure S10a in the SI is shown in Figure S10b in the SI), from which we can see that the fine particle is composed of amorphous nanoclusters. Pulverization and amorphization of the active material would contribute a capacitive capacity to the electrode upon cycling.

Similarly, a phenomenon of the capacity increase with the cycle number for the MoO_3/CNT electrode at a lower current density of 0.2 A g^{-1} can also be observed (see Figure S11 in the SI). For reference, the rate and cycling performances of MoO_3/CNT (WST) are shown in Figures S12 and S13 in the SI, respectively. This sample presents poor rate capability and cycling performance. These results suggest that the synergistic effects of conductivity enhancement and the porous texture may be responsible for the excellent electrochemical performances.

4. CONCLUSIONS

In summary, a MoO_3/MWCNT nanocomposite material was synthesized via a two-step approach. In the first step, a MoO_2/MWCNT precursor was obtained by a CTAB-assisted solvothermal process in a mixed solution of water and ethanol in the presence of MWCNTs. In the second step, the MoO_2/MWCNT precursor was calcined in air at a low temperature of 300 °C for 2 h. The prepared material consists of phase-pure crystalline α-MoO_3 and tightly combined MWCNTs with loose and porous texture. These structural and textural features are highly correlated with the specific preparation procedure. The surfactant CTAB acted as a dispersant as well as a bridging agent to help form a MWCNT-based composite. Besides, the solvothermal process plays an important role in the formation

DOI: 10.1021/acsami.5b03953
ACS Appl. Mater. Interfaces 2015, 7, 15531−15541

of an appropriate MoO_2/MWCNT composite precursor, which is in favor of obtaining a MoO_3/MWCNT composite material with high electrochemical performance. This composite material exhibits high reversible capacity, excellent rate capability, and cyclability as an anode material for the LIB. The excellent rate capability and cycling stability should be attributed to the composite MWCNTs and the porous texture of the composite material.

■ ASSOCIATED CONTENT

Supporting Information

XRD patterns of CNTs, MoO_3/CNT (WST), CTAB, dried intermediates (without CNTs and nitric acid) before and after the solvothermal process, and dried intermediates (without CNTs but with a previous addition of nitric acid) before the solvothermal process, EDS elemental mapping of Mo, O, and C elements for a MoO_3/CNT composite, TG–DSC curves of MoO_2, MoO_2/CNT, and MoO_3/CNT, HRTEM images of the MoO_3/CNT active material before and after 300 cycles at 0.5 A g^{-1}, HRTEM image of a single particle of the MoO_3/CNT active material after 300 cycles at 0.5 A g^{-1}, cycling performance of MoO_3/CNT at 0.2 A g^{-1}, and rate and cycling performances at 0.5 A g^{-1} of MoO_3/CNT (WST). The Supporting Information is available free of charge on the ACS Publications website at DOI: 10.1021/acsami.5b03953.

■ AUTHOR INFORMATION

Corresponding Authors

*E-mail: abyuan@shu.edu.cn. Tel.: +86 21 66138003.
*E-mail: xujiaqiang@shu.edu.cn. Tel.: +86 21 66132701.

Notes

The authors declare no competing financial interest.

■ ACKNOWLEDGMENTS

This work is supported by the National Natural Science Foundation of China (Grant 61371021). The Instrumental Analysis & Research Center of Shanghai University is gratefully acknowledged for XRD, XPS, SEM, TEM, and HRTEM experiments.

■ REFERENCES

(1) Tarascon, J.-M.; Poizot, P.; Laruelle, S.; Grugeon, S.; Dupont, L. Nano-sized Transition-Metal oxides as Negative-Electrode Materials for Lithium-Ion Batteries. *Nature* **2000**, *407*, 496–499.

(2) Xu, S.; Hessel, C. M.; Ren, H.; Yu, R.; Jin, Q.; Yang, M.; Zhao, H.; Wang, D. α-Fe_2O_3 Multi-Shelled Hollow Microspheres for Lithium Ion Battery Anodes with Superior Capacity and Charge Retention. *Energy Environ. Sci.* **2014**, *7*, 632–637.

(3) Xie, D.; Su, Q.; Yuan, W.; Dong, Z.; Zhang, J.; Du, G. Synthesis of Porous NiO-Wrapped Graphene Nanosheets and Their Improved Lithium Storage Properties. *J. Phys. Chem. C* **2013**, *117*, 24121–24128.

(4) Wang, Z.; Chen, J.; Zhu, T.; Madhavi, S.; Lou, X. One-Pot Synthesis of Uniform Carbon-Coated MoO_2 Nanospheres for High-Rate Reversible Lithium Storage. *Chem. Commun.* **2010**, *46*, 6906–6908.

(5) Zhou, L.; Wu, H.; Wang, Z.; Lou, X. Interconnected MoO_2 Nanocrystals with Carbon Nanocoating as High-Capacity Anode Materials for Lithium-ion Batteries. *ACS Appl. Mater. Interfaces* **2011**, *3*, 4853–4857.

(6) Xiao, Q.; Fan, Y.; Wang, X.; Susantyoko, R. A.; Zhang, Q. A multilayer Si/CNT Coaxial Nanofiber LIB Anode with a High Areal Capacity. *Energy Environ. Sci.* **2014**, *7*, 655–661.

(7) Zhou, X.; Bao, J.; Dai, Z.; Guo, Y.-G. Tin Nanoparticles Impregnated in Nitrogen-Doped Graphene for Lithium-Ion Battery Anodes. *J. Phys. Chem. C* **2013**, *117*, 25367–25373.

(8) Xiao, J.; Chen, X.; Sushko, P.; Sushko, M.; Kovarik, L.; Feng, J.; Deng, Z.; Zheng, J.; Graff, G.; Nie, Z.; Choi, D.; Liu, J.; Zhang, J.; Whittingham, M. High-Performance $LiNi_{0.5}Mn_{1.5}O_4$ Spinel Controlled by Mn 3^+ Concentration and Site Disorder. *Adv. Mater.* **2012**, *24*, 2109–2116.

(9) Zhang, X.; Zeng, X.; Yang, M.; Qi, Y. Investigation of a Branchlike MoO_3/Polypyrrole Hybrid with Enhanced Electrochemical Performance Used as an Electrode in Supercapacitors. *ACS Appl. Mater. Interfaces* **2014**, *6*, 1125–1130.

(10) Jiang, F.; Li, W.; Zou, R.; Liu, Q.; Xu, K.; An, L.; Hu, J. MoO_3/PANI Coaxial Heterostructure Nanobelts by In Situ Polymerization for High Performance Supercapacitors. *Nano Energy* **2014**, *7*, 72–79.

(11) Brezesinski, T.; Wang, J.; Tolbert, S. H.; Dunn, B. Ordered Mesoporous α-MoO_3 with Iso-Oriented Nanocrystalline Walls for Thin-Film Pseudocapacitors. *Nat. Mater.* **2010**, *9*, 146–151.

(12) Tang, W.; Liu, L.; Zhu, Y.; Sun, H.; Wu, Y.; Zhu, K. An Aqueous Rechargeable Lithium Battery of Excellent Rate Capability Based on a Nanocomposite of MoO_3 Coated with Ppy and $LiMn_2O_4$. *Energy Environ. Sci.* **2012**, *5*, 6909–6913.

(13) Chen, J.; Cheah, Y.; Madhavi, S.; Lou, X. Fast Synthesis of α-MoO_3 Nanorods with Controlled Aspect Ratios and Their Enhanced Lithium Storage Capabilities. *J. Phys. Chem. C* **2010**, *114*, 8675–8678.

(14) Dong, Y.; Li, S.; Xu, H.; Yan, M.; Xu, X.; Tian, X.; Liu, Q.; Mai, L. Wrinkled-Graphene Enriched MoO_3 Nanobelts with Increased Conductivity and Reduced Stress for Enhanced Electrochemical Performance. *Phys. Chem. Chem. Phys.* **2013**, *15*, 17165–17170.

(15) Wang, G.; Ni, J.; Wang, H.; Gao, L. High-Performance CNT-Wired MoO_3 Nanobelts for Li-Storage Application. *J. Mater. Chem. A* **2013**, *1*, 4112–4118.

(16) Wang, X.-J.; Nesper, R.; Villevieille, C.; Novák, P. Ammonolyzed MoO_3 Nanobelts as Novel Cathode Material of Rechargeable Li-Ion Batteries. *Adv. Energy Mater.* **2013**, *3*, 606–614.

(17) Sakaushi, K.; Thomas, J.; Kaskel, S.; Eckert, J. Aqueous Solution Process for the Synthesis and Assembly of Nanostructured One-Dimensional α-MoO_3 Electrode Materials. *Chem. Mater.* **2013**, *25*, 2557–2563.

(18) Jung, Y. S.; Lee, S.; Ahn, D.; Dillon, A. C.; Lee, S.-H. Electrochemical Reactivity of Ball-Milled MoO_{3-y} as Anode Materials for Lithium-Ion Batteries. *J. Power Sources* **2009**, *188*, 286–291.

(19) Meduri, P.; Clark, E.; Kim, J. H.; Dayalan, E.; Sumanasekera, G. U.; Sunkara, M. K. MoO_{3-x} Nanowire Arrays as Stable and High-Capacity Anodes for Lithium Ion Batteries. *Nano Lett.* **2012**, *12*, 1784–1788.

(20) Yu, X.; Wang, L.; Liu, J.; Sun, X. Porous MoO_3 Film as a High-Performance Anode Material for Lithium-Ion Batteries. *ChemElectroChem* **2014**, *1*, 1476–1479.

(21) Riley, L. A.; Lee, S.-H.; Gedvilias, L.; Dillon, A. C. Optimization of MoO_3 Nanoparticles as Negative-Electrode Material in High-Energy Lithium Ion Batteries. *J. Power Sources* **2010**, *195*, 588–592.

(22) Hassan, M. F.; Guo, Z. P.; Chen, Z.; Liu, H. K. Carbon-Coated MoO_3 Nanobelts as Anode Materials for Lithium-Ion Batteries. *J. Power Sources* **2010**, *195*, 2372–2376.

(23) Wang, Z.; Madhavi, S.; Lou, X. W. Ultralong α-MoO_3 Nanobelts: Synthesis and Effect of Binder Choice on Their Lithium Storage Properties. *J. Phys. Chem. C* **2012**, *116*, 12508–12513.

(24) Feng, C.; Gao, H.; Zhang, C.; Guo, Z.; Liu, H. Synthesis and Electrochemical Properties of MoO_3/C Nanocomposite. *Electrochim. Acta* **2013**, *93*, 101–106.

(25) Yuan, Z.; Si, L.; Wei, D.; Hu, L.; Zhu, Y.; Li, X.; Qian, Y. Vacuum Topotactic Conversion Route to Mesoporous Orthorhombic MoO_3 Nanowire Bundles with Enhanced Electrochemical Performance. *J. Phys. Chem. C* **2014**, *118*, 5091–5101.

(26) Zhou, J.; Lin, N.; Wang, L.; Zhang, K.; Zhu, Y.; Qian, Y. Synthesis of Hexagonal MoO_3 Nanorods and a Study of Their Electrochemical Performance as Anode Materials for Lithium-Ion Batteries. *J. Mater. Chem. A* **2015**, *3*, 7463–7468.

DOI: 10.1021/acsami.5b03953
ACS Appl. Mater. Interfaces 2015, 7, 15531–15541

(27) Ko, Y. N.; Park, S. B.; Kang, Y. C. Excellent Electrochemical Properties of Yolk-Shell MoO_3 Microspheres Formed by Combustion of Molybdenum Oxide-Carbon Composite Microspheres. *Chem. - Asian J.* **2014**, *9*, 1011−1015.
(28) Choi, S. H.; Kang, Y. C. Crumpled Graphene-Molybdenum Oxide Composite Powders: Preparation and Application in Lithium-Ion Batteries. *ChemSusChem* **2014**, *7*, 523−528.
(29) Liu, C.-L.; Wang, Y.; Zhang, C.; Li, X.-S.; Dong, W.-S. In Situ Synthesis of α-MoO_3/Graphene Composites as Anode Materials for Lithium Ion Battery. *Mater. Chem. Phys.* **2014**, *143*, 1111−1118.
(30) Ni, J.; Wang, G.; Yang, J.; Gao, D.; Chen, J.; Gao, L.; Li, Y. Carbon Nanotube-Wired and Oxygen-Deficient MoO_3 Nanobelts with Enhanced Lithium-Storage Capability. *J. Power Sources* **2014**, *247*, 90−94.
(31) Landi, B. J.; Ganter, M. J.; Cress, C. D.; DiLeo, R. A.; Raffaelle, R. P. Carbon Nanotubes for Lithium Ion Batteries. *Energy Environ. Sci.* **2009**, *2*, 638−654.
(32) de las Casas, C.; Li, W. A Review of Application of Carbon Nanotubes for Lithium Ion Battery Anode Material. *J. Power Sources* **2012**, *208*, 74−85.
(33) Aravinda, L. S.; Bhat, U.; Ramachandra Bhat, B. Binder Free MoO_3/Multiwalled Carbon Nanotube Thin Film Electrode for High Energy Density Supercapacitors. *Electrochim. Acta* **2013**, *112*, 663−669.
(34) Yang, P.; Chen, Y.; Yu, X.; Qiang, P.; Wang, K.; Cai, X.; Tan, S.; Liu, P.; Song, J.; Mai, W. Reciprocal Alternate Deposition Strategy Using Metal Oxide/Carbon Nanotube for Positive and Negative Electrodes of High-Performance Supercapacitors. *Nano Energy* **2014**, *10*, 108−116.
(35) Mahmood, Q.; Yun, H. J.; Kim, W. S.; Park, H. S. Highly Uniform Deposition of MoO_3 Nanodots on Multiwalled Carbon Nanotubes for Improved Performance of Supercapacitors. *J. Power Sources* **2013**, *235*, 187−192.
(36) Shakir, I.; Nadeem, M.; Shahid, M.; Kang, D. J. Ultra-Thin Solution-Based Coating of Molybdenum Oxide on Multiwall Carbon Nanotubes for High-Performance Supercapacitor Electrodes. *Electrochim. Acta* **2014**, *118*, 138−142.
(37) Shakir, I.; Shahid, M.; Cherevko, S.; Chung, C.-H.; Kang, D. J. Ultrahigh-Energy and Stable Supercapacitors Based on Intertwined Porous MoO_3−MWCNT Nanocomposites. *Electrochim. Acta* **2011**, *58*, 76−80.
(38) Bhaskar, A.; Deepa, M.; Narasinga Rao, T. MoO_2/Multiwalled Carbon Nanotubes (MWCNT) Hybrid for Use as a Li-ion Battery Anode. *ACS Appl. Mater. Interfaces* **2013**, *5*, 2555−2566.
(39) Li, B.; Han, C.; He, Y.-B.; Yang, C.; Du, H.; Yang, Q.-H.; Kang, F. Facile Synthesis of $Li_4Ti_5O_{12}$/C Composite with Super Rate Performance. *Energy Environ. Sci.* **2012**, *5*, 9595−9602.
(40) Jamnik, J.; Maier, J. Nanocrystallinity Effects in Lithium Battery Materials. *Phys. Chem. Chem. Phys.* **2003**, *5*, 5215−5220.
(41) Zhukovskii, Y. F.; Balaya, P.; Kotomin, E. A.; Maier, J. Evidence for Interfacial-Storage Anomaly in Nanocomposites for Lithium Batteries from First-Principles Simulations. *Phys. Rev. Lett.* **2006**, *96*, 058302.

DOI: 10.1021/acsami.5b03953
ACS Appl. Mater. Interfaces 2015, 7, 15531−15541